

Structure-Activity-Stability Relationships of Pt–Co Alloy Electrocatalysts in Gas-Diffusion Electrode Layers

Shirlaine Koh,[†] Jennifer Leisch,[‡] Michael F. Toney,[‡] and Peter Strasser^{*,†}

Department of Chemical and Biomolecular Engineering, University of Houston, Houston, Texas 77204-4004 and Stanford Synchrotron Radiation Laboratory, Stanford Linear Accelerator Center, Menlo Park, California 94025

Received: November 3, 2006; In Final Form: December 22, 2006

We establish relationships between the atomic structure, composition, electrocatalytic activity, and electrochemical corrosion stability of carbon-supported Pt–Co alloy nanoparticles in electrode catalyst layers. These Pt–Co catalysts have received much attention for use as cathode layers in polymer electrolyte membrane fuel cells (PEMFCs) because of their favorable oxygen-reduction-reaction (ORR) activity and suspected corrosion stability. We reported an enhancement of activity of low-temperature Pt₅₀Co₅₀ of 3 times that of pure carbon supported Pt catalysts. The use of synchrotron X-ray diffraction has enabled structural characterization of the alloy nanoparticles both before and, importantly, after electrocatalysis under fuel cell like conditions. From this, a detailed picture of the relative activity and stability of Pt–Co alloy phases as a function of synthesis conditions has emerged. We have investigated the structure, composition, chemical ordering, and concentration of Pt–Co alloy phases in (i) a dry, freshly synthesized nanoparticle catalyst, (ii) the catalytic electrode layer in a proton-conducting polymer electrolyte before electrocatalytic activity, and (iii) the same electrode layer after electrocatalytic activity. We find that Pt₅₀Co₅₀ catalysts annealed at 600 °C consist of multiple phases: a chemically ordered face-centered tetragonal (fct) and two chemically disordered face-centered cubic (fcc) phases with differing stoichiometries. The Co-rich fcc phase suffers from corrosive Co loss during the preparation of conducting polymer electrode layers and, more significantly, during the ORR electrocatalysis. Most importantly, these fcc phases exhibit high catalytic activities for ORR (about 3× compared to a pure Pt electrocatalyst). Pt₅₀Co₅₀ catalysts annealed at 950 °C consist mainly of the fct Pt₅₀Co₅₀ phase. This phase shows favorable stability to corrosion in the conducting polymer electrode and during electrocatalysis, as the relative intensities of fcc(111)/fct(101) peak ratio remained consistently around 0.5 before and after preparation of conducting polymer electrode layers and before and after electrochemical measurements; however, it exhibits a lower catalytic ORR activity compared to the low-temperature fcc alloy phases (about 2.5× compared to a pure Pt electrocatalyst). Our results demonstrate the complexity in these multiphase materials with respect to catalyst activity and degradation. By understanding of the relationships between crystallographic phase, chemical ordering, composition, and the resulting electrochemical activity and corrosion stability of fuel cell catalysts within polymer-electrolyte/catalyst composites, we can move toward the rational design of active and durable catalyst materials for PEMFC electrodes.

1. Introduction

Direct electrocatalytic conversion of chemical into electric energy using fuel cells offers a number of advantages over conventional energy conversion technologies,^{1–3} most prominently higher conversion efficiency and lower emissions. Among the various fuel cell technologies, low temperature (<200 °C) polymer electrolyte membrane fuel cells (PEMFC) have attracted the most interest because of their flexibility: In the low power regime^{1,4–6} (0.1–100 W), compact liquid PEMFCs, such as direct methanol fuel cells or direct formic acid fuel cells, offer the prospect of uninterrupted power for portable electronics as the fuel cells can be recharged readily with fuel. In the medium to high power regime (0.1–100 kW), hydrogen-based PEMFCs, fed either by a pure hydrogen or a hydrogen rich

reformate gas, hold the promise of a low noise and low emission combined with high efficiency for transportation and stationary power applications. However, to become commercially viable, PEMFCs must overcome high catalyst cost caused by the exclusive use of platinum and platinum alloy catalysts, and limited performance durability, arising mainly from catalyst corrosion, catalyst migration, membrane degradation, and other structural changes associated with the electrocatalytic energy conversion.

At the heart of a PEMFC lies the membrane electrode assembly (MEA), a three-layer structure consisting of a proton-conducting polymer electrolyte layer sandwiched between two mixed-conductivity (electronic and ionic) catalytic gas-diffusion electrodes (anode and cathode). The electrode layers of PEMFCs are complex composite structures with several distinct length scales (Figure 1). They typically consist of a carbon particle-supported (μm scale) high surface area Pt or Pt alloy nanoparticle electrocatalyst (nm scale) on which the electrocatalytic energy conversion occurs.

* Corresponding author. Tel.: +1 713 743 4310. Fax: +1 713 743 4323. E-mail: pstrasser@uh.edu.

[†] University of Houston.

[‡] Stanford Linear Accelerator Center.

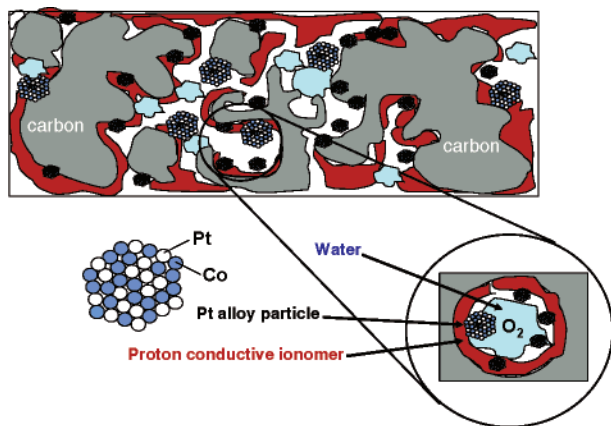
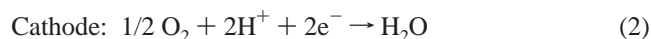


Figure 1. Illustration of the complex structure of a PEMFC gas diffusion electrode layer. The electrode is a composite consisting of carbon supported Pt-alloy nanoparticle catalysts (Pt, white circles; Co, blue circles), a proton-conductive polymeric ionomer (red) such as Nafion, water, and molecular oxygen.

The carbon and metal particles are partially embedded in a proton conducting polymeric ionomer, such as Nafion, which mediates proton migration as well as water transport inside its own pores (supra μm scale). The thickness of such gas-diffusion electrode layers can range from sub μm to about 100 μm . The preparation of these electrode layers is a complex multistep process: The carbon-supported metal nanoparticles are first formulated into a viscous “catalyst ink” using alcoholic solutions of a solubilized proton conducting polymeric ionomer. Subsequently, the catalyst ink is applied to either side of the proton-conducting fuel cell membrane using screen printing, spray, decal transfer, or simply brushing.^{1,7} The final electrode layer constitutes a complex catalytic interface comprising three phases: the solid catalyst metal, liquid water inside and adjacent to the ionomer, and a reactant (hydrogen or oxygen) gas (Figure 1). Partly as a result of this complexity, little is understood about the relationship between the structure, electrochemical activity, and stability of such three-phase interfaces. In particular, the behavior of Pt-alloy nanoparticle catalysts under electrocatalytic operation is largely unexplored.

In a hydrogen/oxygen PEMFC, hydrogen and oxygen gas is fed to the anode and cathode gas-diffusion layers of the MEA, respectively, and a potential difference (cell voltage) develops between the two electrode layers based on the electrochemical processes



However, the observed cell voltage and consequently the performance of the MEA deviate from their theoretical values due to severe kinetic overpotentials at the cathode. The overpotentials are a manifestation of the sluggish rate of adsorption and reduction of molecular oxygen on Pt-alloy cathode electrocatalysts. The identification of more active, cost-effective, and corrosion stable electrocatalysts for the oxygen reduction reaction (ORR) is thus a priority in fuel cell catalysis research. The most popular strategy toward more active and stable ORR electrocatalysts has been alloying pure Pt with selected main group and a variety of transition metals.⁸ Co, Cr, and Ni containing alloys received much attention in the mid-late 1980s^{9–12} and have remained a focus in fuel cell catalysis.^{13–17} There is now a consensus that Pt–Co alloys offer an intrinsic enhancement of electrocatalytic ORR activity on a

Pt mass and surface-area basis. Pt mass based activity enhancements of 1.5–2.5x compared to pure Pt have been reported.^{14–17} The precise mechanistic basis of the enhancement has so far been elusive despite recent progress in combining computational and experimental electrocatalysis.^{18–20} Depending on the method of synthesis and characterization and on the nature of the alloy, various authors have attributed the enhanced activity to alloy lattice geometry,²¹ surface roughness and base metal dissolution,²² electronic effects and orbital occupancy,^{20,23} particle size effects,^{14,24–26} and more recently a “common ion effect” at alloy surfaces.¹⁶

Pt-alloy nanoparticles are known to undergo compositional changes because of leaching and corrosion during catalytic operation in an electrochemical environment.^{27–32} This is particularly true for cathode electrocatalysts that are exposed to potentials of up to +1.1 V/RHE during the electroreduction of oxygen. The leaching detrimentally changes the nanoparticle alloy ORR activity, but despite the importance of this process, the structural changes due to corrosion during the electrocatalytic operation have not been determined. Furthermore, the structural and compositional changes that occur upon contact of the alloy with highly acidic Nafion proton-conducting polymers during the preparation of PEMFC electrodes have not explored so far.^{29,33} Previous attempts to correlate diffraction based structure and activity in ORR alloy electrocatalysts focused on the catalyst structure before electrochemical characterization.^{13,17,34–36} While a few studies consider compositional changes of Pt alloys after treatment in mineral acids,^{30,37} there are no reports addressing structural changes under electrochemical treatment. Hence, relating the activity, structure, and composition of Pt-alloy phases before and after the preparation and electrochemical stressing of PEMFC electrode layers is crucial to furthering our fundamental understanding of the behavior of Pt alloys.

The present paper addresses relationships between the structure, the electrochemical activity, and the corrosion stability of Pt–Co alloy nanoparticles in PEMFC cathodes. We present a detailed analysis of Pt–Co alloy phases in electrochemical fuel cell environments over the lifetime of a cathode catalyst. We start from the state of a freshly synthesized powder and proceed through a stressed Nafion containing electrode. This study answers the question whether chemically ordered or disordered alloy phases are more active or more corrosion stable for PEMFC cathode electrocatalysis.^{16,17,38–42} This work underscores the complexity of multimetallic, multiphase alloy catalysis and takes a step toward atomic-level understanding of Pt-alloy phases in ionomer-containing electrode catalyst layers. Our results provide a better basis for the design of fuel cell electrodes.

2. Experimental

Catalyst Synthesis. Platinum–cobalt catalysts with a Pt–Co stoichiometry of about 75:25 and about 50:50 were synthesized by adding appropriate amounts of solid Co precursor ($\text{Co}(\text{NO}_3)_2 \cdot 6\text{H}_2\text{O}$, Sigma Aldrich No. 239267) to weighted amounts of commercial Pt/carbon electrocatalysts consisting of about 30 wt % platinum supported on a high-surface-area carbon material. Water was added to the supported catalyst powder and the mixture was ultrasonicated until a thick slurry formed (Branson Sonifier 150). The catalyst synthesis mixture was subsequently frozen in liquid nitrogen and then freeze-dried in vacuum (50 mTorr) overnight at room temperature. The resulting fine black powders were annealed to 600 °C (low temperature, “low T” electrocatalyst) and 950 °C (high temperature, “high T” electrocatalyst) for 7 h under 4% hydrogen atmosphere

(Ar balance) and cooled at about 3K/min to room temperature. Fine electrocatalyst powders were obtained, which are well suited for the preparation of catalysts inks and pastes. The final Pt weight loadings of the alloys ranged between 25 and 28 wt % Pt.

Polymer-Electrolyte/Catalyst Electrode Preparation. Rotating disk gas-diffusion catalyst electrodes were prepared following procedures published earlier.^{7,43} Prior to electrode preparation, a 5 mm diameter glassy carbon rotating disk electrode (RDE) (Pine Instruments, AFE2M050GC) was polished to a mirror finish using 0.5 and 0.05 μm alumina suspension (Buehler Inc.). A catalyst ink was prepared by mixing the catalyst powder in 20 mL of an aqueous solution (18.2 M Ω Millipore) containing 5 wt % Nafion solution (Sigma, No. 274704) and isopropyl alcohol. A 10 μL aliquot was dispensed onto the RDE resulting in a typically Pt loading of about 9–14 μg Pt/cm² geometric surface area. The ink was then dried for 10 min in air.

Electrochemical Measurements of Electrode Layers. The electrochemical cell was a custom-made, three-compartment cell containing a glassy carbon working electrode, a mercury–mercury sulfate electrode with a Luggin-Haber capillary. All electrode potentials were converted into the reversible hydrogen electrode (RHE) scale and are reported on this scale. The counter electrode was a piece of platinum gauze to ensure large surface area. A commercial rotator from Pine Instrument was used to conduct the rotating disk experiment. The electrolyte was 0.1 M HClO₄, prepared by diluting 70% redistilled HClO₄ (Sigma No. 311421) with deionized water (>18.2 M Ω , Millipore

Gradient system). The disk potential was controlled with a potentiostat, BiStat (Princeton Applied Research, AMETEK). All measurements were conducted at room temperature. At the beginning of electrochemical measurements, electrocatalysts were immersed into the electrolyte under potential control and held at 0.06 V/RHE until the measurements commenced.

Cyclic voltammetric (CV) was conducted in a deaerated electrolyte under N₂ atmosphere. The electrocatalyst first were pretreated using 200 CV scans between 0.06 and 1.2 V at a scan rate of 500 mV/s. Thereafter, the potential was scanned at 100 mV/s from 0.06 to 1.2 V and back to 0.06 V. The electrochemical platinum surface area (Pt-ESA) of the catalyst was determined from the mean integral charge of the hydrogen adsorption and desorption areas after double-layer correction, using 210 $\mu\text{C}/\text{cm}^2$ as the conversion factor.⁴⁴

Linear sweep voltammetry (LSV) measurements were conducted by sweeping the potential from 0.06 V anodically to the open circuit potential (around 1.0 V) at the scan rate of 5 mV/s. The currents measured were corrected for mass-transport interference. Mass and specific activities were established at 900 mV/RHE at room temperature.

The electrochemical behavior (CV and LSV) of the Pt–Co catalysts was compared to the 30 wt % commercial platinum nanoparticle electrocatalyst used as starting material in the synthesis process.

Compositional Analysis Using Energy Dispersive X-ray Spectroscopy (EDS). Platinum-alloy catalysts powders and electrochemically analyzed catalyst films were deposited on carbon tabs (Ted Pella) and cut to fit the scanning electron

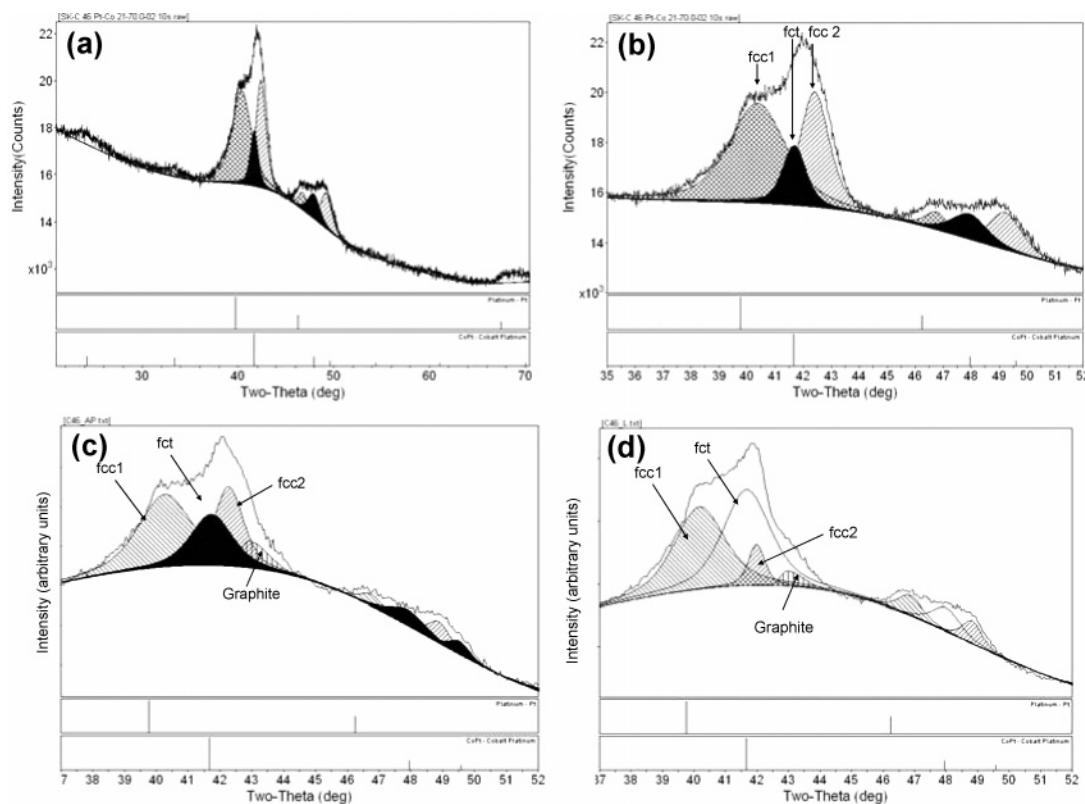


Figure 2. (a) XRD profile and peak analysis of a freshly prepared carbon-supported Pt–Co electrocatalyst powder annealed at 600 °C (low-T catalyst). Cross-hatched and diagonal reflections indicate the fcc phases, dark peaks indicate the fct Pt₅₀Co₅₀ phase. Overall compositions of the catalyst are listed in Table 1. (b) Enlarged XRD profile of (a). “fcc1”, “fcc2”, and “fct” indicate the main reflections of the disordered fcc and the ordered fct phases, respectively. Overall compositions of the catalyst are listed in Table 1. (c) XRD profile and peak profile analysis of a carbon paper supported Nafion-containing electrode layer containing the low-T catalyst powder of (a). The electrode film was not exposed to electrochemical potential or electrochemical testing. Labels “fcc” and “fct” follow the nomenclature in (b). (d) XRD profile and peak analysis of the Nafion-containing electrode layer from (c) after application of an electrochemical stress protocol for ORR. 0.1 M HClO₄, 25 °C. For details of the electrochemical protocol, refer to the experimental section.

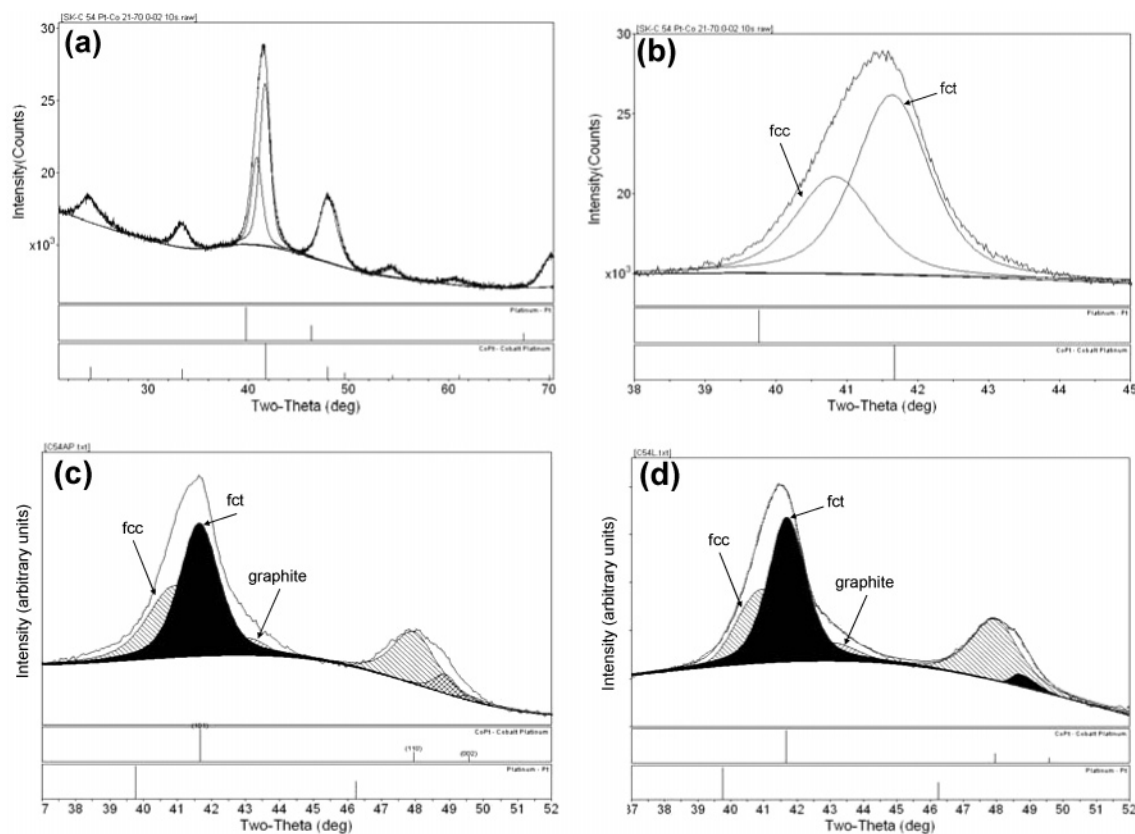


Figure 3. (a) XRD profile and peak analysis of a freshly prepared carbon-supported Pt–Co electrocatalyst powder annealed at 950 °C (high-T catalyst). (b) Enlarged XRD profile of (a). “fcc” and “fct” indicate the main reflections of the disordered fcc and the ordered fct phases, respectively. Overall compositions of the catalyst are listed in Table 1. (c) XRD profile and peak analysis of a carbon paper supported Nafion-containing electrode layer containing the high-T catalyst powder of (a). The electrode film was not exposed to electrochemical potential or electrochemical testing. Labels “fcc” and “fct” follow the nomenclature in (b). (d) XRD profile and peak analysis of the Nafion-containing electrode layer from (c) after application of an electrochemical stress protocol for ORR. 0.1 M HClO₄, 25 °C. For details of the electrochemical protocol, refer to the experimental section.

microscope (SEM) specimen mounts. EDS analysis was performed using a JEOL JSM 6330F field emission SEM with resolution of 1.5 nm with potential of 15.0 kV, current of 12 μ A, and working distance of 15 mm. Alloy samples of known composition were used for calibration. About 5–10 spots across the catalyst film were probed and an average of these compositions was determined. The experimental precision associated with the EDS method was estimated to be about 3 atom %.

Structure Analysis Using Laboratory-Based X-ray Diffraction (XRD). Laboratory-source X-ray diffraction was conducted using a Siemens D5000 ($\theta/2\theta$) diffractometer (Bragg Brentano configuration, Cu K α source) equipped with a Braun position sensitive detector (PSD) with an angular range of 8°. Composition estimations of substitutionally disordered face-centered cubic (fcc) Pt–Co alloy phases were based on a near-linear relationship between molar Co content and size of resulting lattice parameters. All X-ray diffraction patterns were analyzed using Jade 7.5 of Material Data, Inc. (MDI): peak profiles of individual reflections were obtained by a nonlinear least-square fit of the Cu K α_2 corrected data. Instrumental broadening was determined by a standard powder sample under identical measurement conditions.

Structural Analysis Using Synchrotron-Based XRD. Pt–Co/Nafion catalyst films were analyzed structurally after electrochemical testing using Synchrotron based XRD. Diffraction measurements were conducted at the Stanford Synchrotron Radiation Laboratory (SSRL) at beamline 2-1 using radiation of $\lambda = 1.5505$ Å. Sample films were mounted vertically onto the goniometer head and measured in transmission (θ – 2θ

configuration). Detector collimation was 2 mrad Soller slits. A scintillation detector collected data between 2θ of 20° and 100°, using step scans of 0.02°/step and a counting time of 2–3 s per step. The raw data was converted into Cu K alpha wavelength of $\lambda = 1.5418$ Å to enable comparison with lab data.

3. Results and Discussion

Structural Analysis of Pt₅₀Co₅₀ Alloy Powder Electrocatalysts. Carbon-supported Pt–Co alloy nanoparticles with nominal stoichiometry of Pt₅₀Co₅₀ were synthesized using low (600 °C) and high (950 °C) temperature annealing (low T and high T catalysts). This section addresses their initial phase structure and composition as freshly synthesized catalyst powders. Figures 2a,b and 3 a,b show the deconvoluted XRD profiles of the two catalysts over the full 2θ range and near the fcc (111) and (200) peaks. Details on the symmetry, particle size, composition, and relative ratios of the observed phases are summarized in Table 1 (“dry powder”).

The low-T catalyst exhibits three distinct alloy phases: one chemically ordered intermetallic and two chemically disordered random alloys. The phase referred to as “fcc 1” and marked with cross-hatched fundamental reflections in Figure 2b is a Pt-rich fcc phase with an estimated composition of Pt₈₅Co₁₅. The Pt–Co phase compositions for fcc alloys were obtained assuming a linear relationship between the Co concentration and the lattice constant. Also present are a Co rich fcc phase (referred to as “fcc 2” and marked with diagonal hatched reflections in Figure 2b) (Pt₃₈Co₆₂) and a chemically ordered

TABLE 1: Overview of Synthesis Conditions, Crystallographic Structural Characteristics, and Compositional Data of the High T and Low T Pt-Co Electrocatalysts

	EDS catalyst comp	synthesis temp (°C)	annealing time (h)	figure	catalyst format	alloy phase label	alloy phase symmetry	phase composition Pt/Co	lattice parameters a/c (Å/Å)	particle size (nm)	relative intensity of fcc1(111)/PtCo(101) peaks	relative intensity of fcc2(111)/PtCo(101) peaks
before testing	Pt/Co 37:63	600	7	1a,b	dry powder	fcc1	disordered fcc <i>Fm3m</i>	85:15	3.867/3.867	3.51		
						fct	ordered fct <i>P4/mmm</i>	50:50	2.682/3.675	8.91	1.55	1.71
						fcc2	disordered fcc <i>Fm3m</i>	38:62	3.690/3.690	7.14		
	Pt/Co 50:50	600	7	1c	catalyst/ionomer thin film	fcc1	disordered fcc <i>Fm3m</i>	88:12	3.876/3.876	4.31		
						fct	ordered fct <i>P4/mmm</i>	50:50	2.682/3.675	5.54	1.41	1.54
						fcc2	disordered fcc <i>Fm3m</i>	41:59	3.700/3.700	7.84		
	Pt/Co 41:59	950	7	2a,b	dry powder	fcc	disordered fcc <i>Fm3m</i>	73:27	3.819/3.819	5.94		
						fct	ordered fct <i>P4/mmm</i>	50:50	2.682/3.675	6.45	0.52	
	Pt/Co 46:54	950	7	2c	catalyst/ionomer thin film	fcc	disordered fcc <i>Fm3m</i>	72:28	3.818/3.818	4.58		
						fct	ordered fct <i>P4/mmm</i>	50:50	2.682/3.675	6.13	0.54	
after testing	Pt/Co 60:40	600	7	1d	catalyst/ionomer thin film	fcc1	disordered fcc <i>Fm3m</i>	90:10	3.884/3.884	7.45		
						fct	ordered fct <i>P4/mmm</i>	50:50	2.682/3.675	8.5	0.86	0.43
						fcc2	disordered fcc <i>Fm3m</i>	47:53	3.724/3.724	5.73		
	Pt/Co 52:48	950	7	2d	catalyst/ionomer thin film	fcc	disordered fcc <i>Fm3m</i>	71:29	3.814/3.814	5.21		
						fct	ordered fct <i>P4/mmm</i>	50:50	2.682/3.675	5.82	0.51	

face-centered tetragonal (fct) phase⁴⁵ (marked as “fct” in Figure 2b) with Pt₅₀Co₅₀ composition. The (001) and (100) superlattice reflections at low angles (24 and 33° 2θ, respectively) confirm the formation of the fct phase. The fcc(111)/fct(101) peak ratios of 1.55 and 1.71 for fcc1 and fcc2 (see Table 1) show that the fcc phases are prevalent at low temperatures.

In contrast to the multiphase structure of Figure 2a,b, high-T annealing results in a more uniform phase structure (Figure 3a,b and Table 1). The alloy catalysts consist mainly of the fct Pt₅₀Co₅₀ phase with some contribution of a Pt-rich fcc phase (Pt₇₃Co₂₇).

The observed structural data is consistent with earlier findings in which fct Pt₅₀Co₅₀ lattices start forming at and above annealing temperatures of 600 °C.^{17,33} We speculate that in the annealing process, small Pt-metal particles are initially present next to amorphous Co nitrate domains. After decomposition of the nitrate anions at around 250 °C, Co oxide is formed. At higher temperatures, Co-oxides are reduced to metallic Co. The reductive annealing process forms large Co crystallites that then diffuse into the pure Pt particles to form alloy phases of varying compositions. On the basis of this mechanism, Co-rich phases are larger in size than Pt richer phases. In the range of 600–950 °C⁴⁶, the highly mobile Co and Pt atoms start forming disordered and thermodynamically preferred chemically ordered phases. Although there are only two data points, the amount of chemical ordering increases with annealing temperature, as seen from the relative peak intensities of the main reflections of the fcc and fct phases (Table 1). Many earlier studies^{33,47} employing reductive annealing synthesis failed to acknowledge the multiphase nature of Pt–Co particle catalysts. In fact, our detailed peak profile analysis underscores that despite sustained high temperatures, single phase materials are rather difficult to obtain.

The multiphase nature of electrocatalysts offers the unique opportunity to evaluate side-by-side the relative stability of chemically disordered and ordered phases.

Structure and Stability of Pt₅₀Co₅₀ Alloys during Preparation of Nafion-Containing Electrode Layers. For the preparation of catalytic gas-diffusion electrodes, the high-T and low-T Pt₅₀Co₅₀ electrocatalysts were formulated into aqueous “catalyst inks” using isopropyl alcohol/water mixtures. To enable protons to migrate to the catalyst surface and react with oxygen to form water, a solubilized Nafion proton-conductive-polymer was added to the catalyst ink formulation. To prepare catalytic electrodes on smooth glassy carbon (GC) disk electrodes, an aliquot of ink was dispensed and dried onto the GC surface. Aqueous protonated Nafion solutions contain highly acidic sulfonates groups and, consequently, exhibit a very low pH around 1.¹ To investigate the stability of Pt–Co alloy phases after formulation of electrode layers, synchrotron-based X-ray diffraction profiles were recorded using the gas-diffusion Nafion/catalyst layers supported on graphitic carbon paper. Figures 2c and 3c show the diffraction profiles of the low-T and high-T electrocatalyst, respectively, and Table 1 reports the corresponding compositional and structural analysis. For the low-T Pt₅₀Co₅₀ catalyst, there is a drop in peak intensities of the two fcc phases, fcc1 and fcc2, compared to the fct phase. Also, the disordered phases display a shift in composition toward lower Co content (see Table 1, column 9). These changes are in line with the EDS-based compositional analysis that indicates an overall loss of 13 atom % Co. The particle sizes of the fct phase also remained consistently constant before and after electrochemical testing. The drop in the fct phase particle size in the catalyst/ionomer thin film was most likely due to the positioning of the fct phase between the two fcc phases. As such, fitting

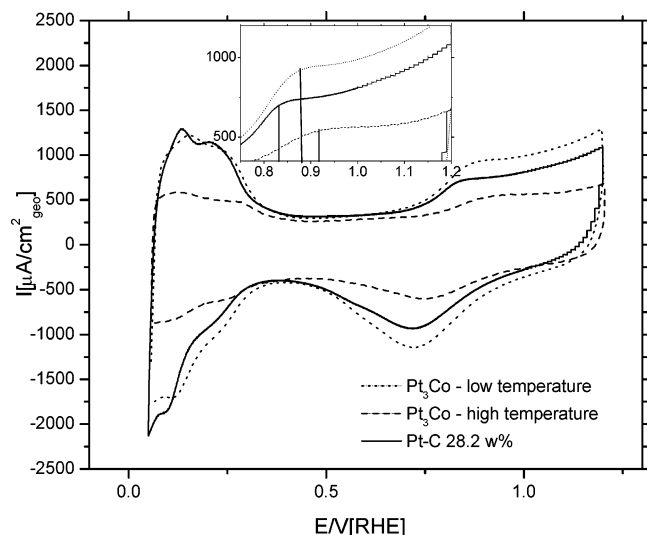


Figure 4. CV profiles (100 mV/s) of the high-temperature and low-temperature Pt₇₅Co₂₅ alloy catalysts after electrochemical conditioning. For comparison, the CV profile of a Pt-reference catalyst is given. Inset shows a blow-up of the potential region in which water activation and Pt–OH formation occur.

the fct phase would amount to larger uncertainties than the fcc phases. These results all point to preferred corrosion of the disordered phases, fcc1 and fcc2, compared to the fct phase.

In the high-T Pt₅₀Co₅₀ catalyst, virtually no change in peak position, phase composition, particle sizes, or relative intensity is detected, consistent with the small loss of about 4 atom % Co. Hence, chemically ordered fct Pt₅₀Co₅₀ crystallographic phases are more corrosion resistant in acidic polymer electrolyte ionomer environments and represent the preferred phase structure under stability considerations. This is one significant result of this paper.

Hydrogen and Water Adsorption Characteristics of Pt–Co Alloy Nanoparticles. The following two sections address the electrocatalytic activity of Pt₅₀Co₅₀-alloy catalysts with respect to ORR inside the Nafion electrode layers. A comparative kinetic analysis is presented of the low-T and high-T Pt₅₀Co₅₀ catalysts and similarly prepared Pt₇₅Co₂₅ catalysts. The catalysts were preconditioned using 200 fast CV cycles,^{1,48–50} followed immediately by a slow (100 mV/s) cycle. Figures 4 and 5 show the slow CV cycles of the Pt₇₅Co₂₅ (denoted as “Pt₃Co”) in Figures 4–7) and the Pt₅₀Co₅₀ (denoted as “PtCo”) in Figures 5–7), respectively. Also depicted is the response of a pure Pt-reference catalyst. The voltammetric features in the 0.05–0.4 V represent the adsorption and desorption of a monolayer of hydrogen atoms on top of Pt surface atoms. These features are used to estimate the electrochemical Pt surface areas of the individual catalysts.

Distinct CV behavior arises for the low-T versus the high-T catalysts: the low-T catalyst exhibits a hydrogen adsorption charge comparable to the Pt-reference catalyst suggesting a large number of available Pt-surface atoms. In fact, normalizing by the mass of Pt in the electrode layer, the Pt-ESA of the Pt₅₀Co₅₀ catalyst is about 69 m²/g_{Pt}, similar to the 77 m²/g_{Pt} obtained for the reference catalyst. These data confirm incomplete alloying with the presence of a Pt-rich alloy phase, as found in Figure 2c. In contrast, high-T powders show a CV with reduced interfacial capacitance and a significantly reduced hydrogen adsorption charge; the Pt-ESA of these catalysts is only 28 m²/g_{Pt}. Because the mean particle sizes (obtained from the (111) peak widths using the Scherrer expression^{51,52}) of the low-T and high-T Pt₅₀Co₅₀ are comparable (Table 1), the

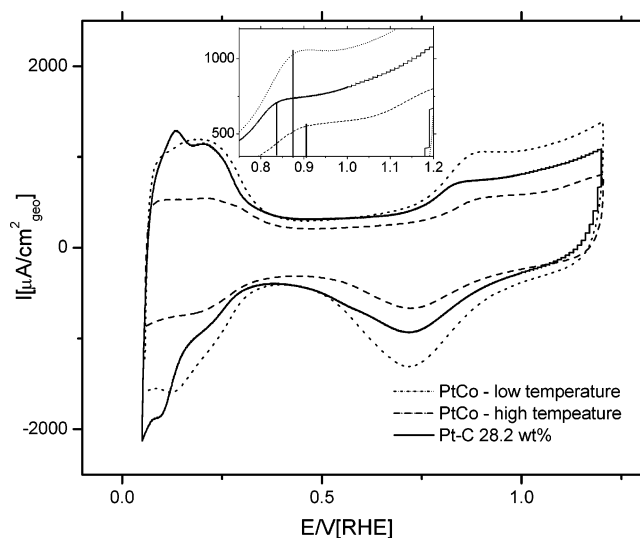
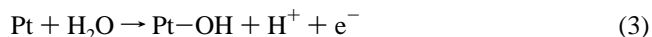


Figure 5. CV profiles (100 mV/s) of the high-temperature and low-temperature Pt₅₀Co₅₀ alloy catalysts after electrochemical conditioning. For comparison, the CV profile of the Pt-reference catalyst is given. Inset shows a blow-up of the potential region in which water activation and Pt–OH formation occur.

changes in the Pt-ESA is likely due to a reduced number of Pt atoms in the top layer (possibly because of Co surface enrichment), consistent with previous conjectures for Pt–Co alloy surfaces.¹⁶

Relevant to a kinetic analysis of the Pt–Co catalysts is the onset and peak potential of the activation of water molecules in the range of 0.7–0.9 V/RHE (see inserts in Figures 4 and 5). Water adsorption and subsequent activation results in oxygenated surface species such as Pt–OH and Pt–O



These species have two effects: (1) they decrease the number of available surface area for oxygen adsorption and reduction and (2) they modify the apparent Gibbs energy of adsorption, ΔG_{ad} ,^{16,53} for oxygenated surface species (Temkin adsorption conditions).^{48,54,55} In accordance to a recently proposed model for the rate expression for ORR,^{16,49} the first effect reduces the observed oxygen reduction currents by a $(1-\theta_{\text{ad}})$ term in the rate law, with θ_{ad} denoting the total surface coverage of adsorbed species. The same model predicts that the second effect causes curved rather than linear electrochemical Tafel plots (plots of applied potential versus the log of the catalytic activity (e.g., Figure 6)).^{16,34,56,57} Curvature is predicted below the potential where the pseudocapacitive process of reaction (3) causes a current plateau in the CV (0.8–0.9 V), while linear Tafel plots are predicted at higher potentials.

The inserts in Figures 4 and 5 show the enlarged potential region in which reaction (3) occurs. We observe the following order in the current plateaus: E_{peak} (high-T alloys) (~ 0.9 V) > E_{peak} (low-T alloys) (~ 0.85 V) > E_{peak} (Pt) (~ 0.82 V). According to the kinetic model mentioned above^{35,49} this is also the predicted order in which the Tafel plots should exhibit curvature. This behavior is discussed in the next section. In summary, from the results of the CVs we conclude that the low-T and high-T Pt₅₀Co₅₀ and Pt₇₅Co₂₅ catalysts will have a high ORR activity because of the delayed onset of water adsorption and activation (i.e., a large number of available adsorption sites $(1-\theta_{\text{ad}})$ for molecular oxygen).

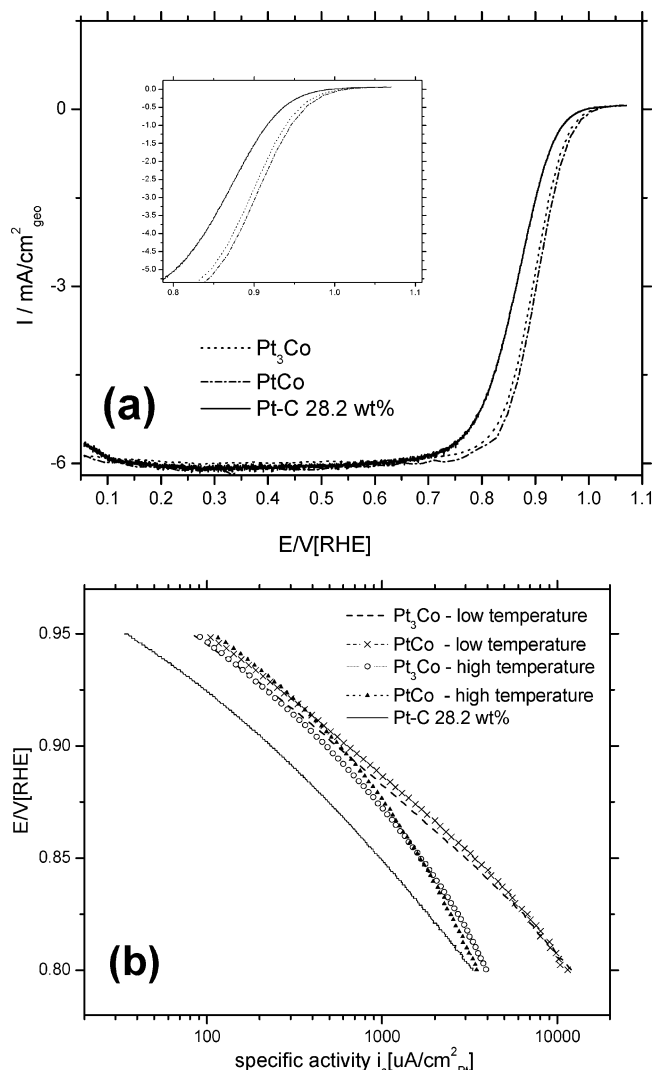


Figure 6. (a) LSV of the Pt₇₅Co₂₅ and Pt₅₀Co₅₀ catalysts compared to the Pt-reference catalyst. Inset: blow-up of the 900 mV/RHE region. (b) Tafel plot of the Pt surface area normalized current density (specific activity) of Pt₇₅Co₂₅ and Pt₅₀Co₅₀ alloys compared to the reference Pt electrocatalyst.

Electrocatalytic Characterization of Pt–Co Nanoparticle Catalysts. Figure 6a compares the voltammetric anodic sweeps of the low-T Pt₅₀Co₅₀ and Pt₇₅Co₂₅ catalysts in the gas diffusion cathode layers. The high-T sweeps look similar and are omitted. The diffusion-limited current (0.1–0.8 V range) is consistent with earlier reports for the 4-electron reduction pathway.⁷ All four Pt–Co materials exhibit a significant activity advantage over the reference Pt catalyst as indicated by the early ORR onset potential of about 1.0 V/RHE. Figure 6b shows the electrochemical Tafel plot using the Pt surface-area specific activity, which is the mass-transport corrected^{7,58} ORR currents at 0.9 V/RHE normalized by the electrochemical Pt surface area, Pt-ESA (obtained from the CVs in Figures 4 and 5). The Pt-ESA specific activity is the intrinsic catalytic activity of the nanoparticle surface and is related to the turn-over-number commonly cited in the heterogeneous gas-phase catalysis literature.⁷ Figure 7 compares the average specific activities at 0.9 V obtained for the Pt₅₀Co₅₀ and Pt₇₅Co₂₅ alloys. The activities reported here are consistent with those reported previously.^{7,20} These data show an ORR activity increase for the low-T Pt₅₀Co₅₀ catalyst of a factor of 3 compared to pure Pt. This is one of the highest electrochemical ORR activities reported to date.^{7,16,17,20,34,59,60} The electrochemical ORR activities for Pt₅₀-

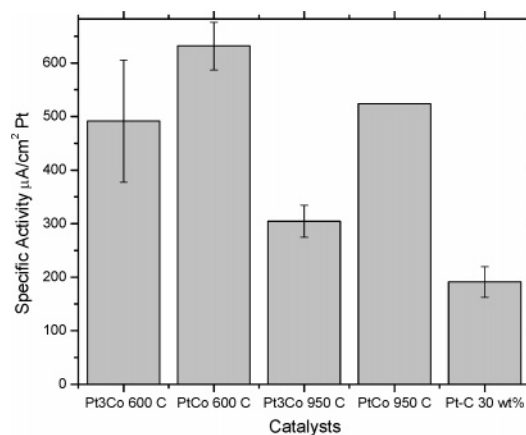


Figure 7. Specific activities of the two Pt₇₅Co₂₅ (= Pt₃Co) alloys, the two Pt₅₀Co₅₀ (= PtCo) alloys, and the reference Pt electrocatalysts at 900 mV/RHE.

Co₅₀ catalyst were higher than Pt₇₅Co₂₅ for both low T and high T. This observation is consistent with the data reported earlier.^{16,34}

To understand the observed activity trends, it should first be noted that Pt-ESA-based specific activities of particle catalysts are generally independent of particle dispersion and the number of active Pt surface sites. Often the concept of the “particle size effect”⁷ is invoked to explain Pt ORR electrocatalysis results. This concept states that Pt particle size correlates with the specific ORR activity, because smaller Pt particles have a higher density of surface defects (kinks and steps) where water tends to be rapidly activated thereby blocking surface sites for oxygen adsorption and reducing the ORR activity.^{7,32} The particle size effect concept is inconsistent, however, with our experimental data: high-T annealing results in larger mean particle sizes and should therefore lead to higher activity. This is opposite to our observations (see Figure 7). In addition, Table 1 shows that the mean particle sizes of the two Pt₅₀Co₅₀ catalysts are comparable. Hence, particle size effects cannot account for the observed activity trends.

Instead, we believe that the crystallographic structures of some of the phases in low-T Pt₅₀Co₅₀ catalyst possess a high intrinsic ORR activity. Comparing the structural results from Figure 2 with the specific activity in Figure 7 suggests that the mixture of a Pt-rich and a Co-rich chemically disordered fcc phase results in a more active ORR catalyst than the predominantly ordered fct phase of the high-T Pt₅₀Co₅₀ catalyst or than pure Pt. Even though it is less corrosion stable during the preparation of electrode films, chemically disordered fcc Pt–Co phases appear to offer more active catalytic surface sites and are the preferred catalyst materials from the standpoint of specific ORR activity. The favorable activity of fcc Pt–Co phases is a significant experimental finding. It suggests a stronger focus on low-temperature or high-quenching type alloy preparation methods that are likely to favor chemically disordered alloys.^{27,46}

Returning to the kinetic discussion of the onset of Temkin type adsorption, Figure 6b shows that the changes in Tafel slopes are in agreement with the kinetic conjectures from the previous section: starting from the highest potentials, the Tafel slopes of the high-T Pt–Co catalysts show early deviations from linearity ($E = 0.9$ V), followed by the low-T Pt–Co catalysts ($E = 0.83$ V), and then pure Pt ($E < 0.83$ V). On Pt–Co-alloy surfaces, detrimental oxygenated surface species from water form at higher electrode potentials compared to pure Pt and therefore the Pt–Co alloys benefit kinetically from a larger

number of available surface sites for oxygen adsorption, that is a larger $(1-\theta_{ad})$ term in the rate law.^{16,49}

Structure and Stability of Pt₅₀Co₅₀ Alloys in Nafion-Containing Electrode Layers after Electrocatalysis. Figures 2d and 3d report, respectively, the diffraction patterns of the low-T and high-T Pt₅₀Co₅₀ catalysts after the electrochemical ORR, and Table 1 summarizes our analysis. Peak profile analysis of the low-T catalyst (Figure 2d) points again to the presence of two disordered fcc phases (fcc1, fcc2) and the chemically ordered fct Pt₅₀Co₅₀ phase. While the compositions of the individual alloy phases are slightly changed compared to the initial conditions, their relative distribution has changed significantly. The fcc2 alloy composition changed from Pt₄₁Co₅₉ to Pt₄₇Co₅₃ indicating corrosive loss of Co atoms most likely from the nanoparticle surface and possibly the interior. As a consequence, the Pt–Co surface is roughened, as seen from the increase in Pt-ESA to 75 m²/g_{Pt} from the previous 69 m²/g_{Pt}. The fcc1 phase has a composition of about Pt₉₀Co₁₀, suggesting only a small compositional change. Most importantly, there is a large drop in the relative fcc2(111)/fct(101) peak intensities from 1.5 to 0.43; this points to a preferred corrosion of the fcc2 phase during ORR electrocatalysis compared with the chemically ordered fct. Similarly, the peak intensity ratio between the fcc1 and fct phase decreases from 1.41 to 0.86, suggesting corrosion of the Pt-rich fcc phase. These changes in the distribution of alloy phases are qualitatively consistent with the overall compositional reduction of Co by about 10 atom % as reported in the first column of Table 1.

In summary, the postreaction data confirms the enhanced stability of the chemically ordered fct Pt₅₀Co₅₀ phase in catalytic electrodes. This is perhaps not surprising as the fct phase is thermodynamically stable compared to the fcc phases. The mean particle sizes (Table 1) indicate that the preferred leaching of the fcc2 phase causes a decrease in fcc2 particle size, while the particle sizes for the other two phases tend to grow under ORR. A decrease in particle size could be indicative of a corrosion process that preferably removes Co atoms from the alloy lattice and eventually leads to a break-up and, consequently, a size reduction of the Co-rich alloy particles; this hypothesis is consistent with recent X-ray scattering results on Pt–Co and Pt–Cu alloy particles.²⁹

Peak profile analysis of the high-T catalyst (Figure 3d) shows that the ordered fct Pt₅₀Co₅₀ phase continues to be the primary phase (Table 1). In contrast to the low-T catalyst, the distribution of the alloy phases is virtually unchanged after ORR. Furthermore, the (111)/(101) peak intensity ratio is 0.5 unchanged from the pre-ORR ratio, suggesting no significant preferred leaching of either phase. As the overall catalyst composition after electrochemistry indicates a Co loss of about 6 atom %, all phases appear to have leached uniformly. The Pt-ESA increases only slightly, consistent with the compositional and structural data and in contrast with the low-T material. The high-T analysis corroborates the favorable stability to corrosion of chemically ordered fct Pt₅₀Co₅₀ phases. Particle size considerations (Table 1) show that the high-T alloy phases, aside from being more corrosion stable, are also more resistant to growth and sintering.

Previous corrosion stability studies of Pt alloys addressed changes in the Pt-ESA and activity alone or considered purely compositional changes of the catalytic material before and after electrocatalysis.^{7,17,30,32,35,61–69} Relevant to the present discussion is a study of the corrosion stability of a chemically ordered fct Pt₅₀Fe₅₀ catalyst⁷⁰ that evidenced little compositional change of the fct phase after chemical immersion in 0.5 M aqueous H₂SO₄. While this is in line with the present results, it should

be noted that acid treatment is a purely chemical corrosion test under open circuit conditions and does not well represent the more severe corrosive environments of an electrified interface under ORR. Another study³⁰ reports a series of Pt₇₅Co₂₅ alloy catalysts that were investigated with respect to their compositional stability before and after use in a PEMFC. Similar to the results presented here, the overall composition dropped by about 5–7 atom % Co, but no structural data were provided after electrochemical stressing.

4. Summary

We have correlated structure, composition, and electrochemical behavior of carbon-supported Pt–Co alloy electrocatalysts for use in PEMFC cathode electrode layers and have established a number of detailed structure–property relations for this class of materials. Using synchrotron XRD, we have investigated these relations during the typical life-cycle of a PEMFC cathode catalyst: (i) freshly prepared catalyst powder, (ii) inside a catalyst/Nafion-ionomer electrode layer, and (iii) inside an electrocatalytically stressed Nafion-ionomer electrode layer.

Low-temperature preparation conditions favor the formation of multiple primarily fcc Pt–Co alloy phases of various stoichiometries. The Co-rich fcc phases suffer from severe chemical and electrochemical corrosion, but are associated with the most favorable ORR activities of up to 3× the specific activity of pure Pt catalysts. The kinetic advantage of the leached fcc Pt–Co alloy phases has been linked to a delayed onset of the formation of oxygenated adsorbates from water, such as Pt–OH, on these alloy phases. The present kinetic analysis is in favorable agreement with predictions of a suggested rate expression⁷¹ for the ORR. Chemically disordered fcc alloy phases, particularly those with initially high Co content (>50 atom %), are the desired materials for highly active PEMFC cathodes. We suspect that their preferred leaching is an integral part of their high intrinsic activity.

High-temperature preparation conditions for carbon-supported Pt₅₀Co₅₀ catalysts favor the formation of chemically ordered fct Pt₅₀Co₅₀ alloy phase. Hydrogen adsorption analysis indicates that high-T annealing favors the surface enrichment Co atoms in these materials. While catalytically less active, fct Pt–Co phases have shown a favorable, though not a complete, stability to electrochemical corrosion in Nafion-containing electrode layers before and after electrochemical stress. Chemically ordered fct Pt₅₀Co₅₀ alloy phases are the desired materials for stable PEMFC cathodes.

The present study underscores the complexity and trade-offs with regards to catalyst activity and degradation in multiphase materials. It constitutes an important step toward atomic-level characterization and understanding of the behavior of the crystallography of Pt-alloy phases inside ionomer-containing electrode layers; the results are of both fundamental and practical interest to our understanding of the activity–durability relationships of catalyst materials in PEMFC environments.

Acknowledgment. This project is supported by the Department of Energy, Office of Basic Energy Sciences (BES), under Grant LAB04-20; by the Texas Center for Superconductivity at the University of Houston (TcSUH); by the American Chemical Society Petroleum Fund (ACS-PRF #44165-G5), and by the seed grants (GEAR) provided by the University of Houston. Portions of this research were carried out at the Stanford Synchrotron Radiation Laboratory, a national user facility operated by Stanford University on behalf of the U.S. Department of Energy, Office of Basic Energy Sciences.

References and Notes

- (1) *Handbook of Fuel Cells - Fundamentals, Technology, and Application*; Vielstich, W.; Lamm, A.; Gasteiger, H., Eds.; Wiley: New York, 2003.
- (2) Larminie, J.; Dicks, A. *Fuel Cell Systems Explained*; Wiley: New York, 2000.
- (3) O'Hayre, R.; Cha, S.-W.; Colella, W.; Prinz, F. B. *Fuel Cell Fundamentals*; Wiley: New York, 2006.
- (4) Heller, A. *Phys. Chem. Phys.* **2004**, *6*, 209–216.
- (5) Wasmus, S.; Kuver, A. *J. Electroanal. Chem.* **1999**, *461*, 14–31.
- (6) Dyer, C. K. *J. Power Sources* **2002**, *106*, 31–34.
- (7) Gasteiger, H. A.; Kocha, S. S.; Sompalli, B.; Wagner, F. T. *Appl. Catal., B* **2005**, *56*, 9–35.
- (8) Stonehart, P. *Phys. Chem* **1990**, *94*, 913–921.
- (9) Beard, B. C.; Ross, P. N. *J. Electrochem. Soc.* **1990**, *137*, 3368–3374.
- (10) Luczak, F. J.; Landsman, D. A. Ternary Fuel Cell Catalysts Containing Platinum, Cobalt and Chromium. U.S. Patent 4,447,506, 1984.
- (11) Luczak, F. J.; Landsman, D. A. Ordered Ternary Fuel Cell Catalysts Containing Platinum and Cobalt. U.S. Patent 4,711,829, 1987.
- (12) Luczak, F. J.; Landsman, D. A. Ordered Ternary Fuel Cell Catalysts Containing Platinum and Cobalt and method for making the Catalyst. U.S. Patent 4,677,092, 1987.
- (13) Antolini, E.; Salgado, J. R. C.; Giz, M. J.; Gonzalez, E. R. *Int. J. Hydrogen Energy* **2005**, *30*, 1213–1220.
- (14) Min, M.-k.; Cho, J.; Cho, K.; Kim, H. *Electrochim. Acta* **2000**, *45*, 4211–4217.
- (15) Mukerjee, S.; Srinivasan, S.; Soriaga, M.; McBreen, J. *Phys. Chem.* **1995**, *99*, 4577.
- (16) Paulus, U. A.; Wokaun, A.; Scherer, G. G.; Schmidt, T. J.; Stamenkovic, V.; Radmilovic, V.; Markovic, N. M.; Ross, P. N. *J. Phys. Chem. B* **2002**, *106*, 4181–4191.
- (17) Xiong, L.; Manthiram, A. *J. Electrochem. Soc.* **2005**, *152*, A697–A703.
- (18) Norskov, J. K.; Rossmeisl, J.; Logadottir, A.; Lindqvist, L.; Kitchin, J. R.; Bligaard, T.; Jonsson, H. *J. Phys. Chem. B* **2004**, *108*, 17886–17892.
- (19) Strasser, P.; Fan, Q.; Devenney, M.; Weinberg, W. H.; Liu, P.; Norskov, J. K. *J. Phys. Chem. B* **2003**, *107*, 11013.
- (20) Stamenkovic, V.; Moon, B. S.; Mayerhofer, K. J.; Ross, P. N.; Markovic, N.; Rossmeisl, J.; Greeley, J.; Norskov, J. K. *Angew. Chem., Int. Ed.* **2006**, *45*, 2897–2901.
- (21) Jalan, V. M.; Taylor, E. J. *J. Electrochem. Soc.* **1983**, *130*, 2299–2301.
- (22) Paffett, M. T.; Beery, J. G.; Gottesfeld, S. *J. Electrochem. Soc.* **1988**, *135*, 1431.
- (23) Mukerjee, S.; Srinivasan, S.; Soriaga, M. P.; McBreen, J. *J. Electrochem. Soc.* **1995**, *142*, 1409–1422.
- (24) Kinoshita, K. *J. Electrochem. Soc.* **1990**, *137*, 845.
- (25) Mukerjee, S. *J. Appl. Electrochem.* **1990**, *20*, 537–548.
- (26) Bregoli, L. *J. Electrochim. Acta* **1978**, *23*, 489.
- (27) Watanabe, M.; Tsurumi, K.; Mizukami, T.; Nakamura, T.; Stonehart, P. *J. Electrochem. Soc.* **1994**, *141*, 2659–2668.
- (28) *Corrosion - Understanding the Basics*; Davis, J. R., Ed.; ASM International: Materials Park, Ohio, 2000.
- (29) Koh, S.; Leisch, J.; Toney, M. F.; Strasser, P. Presented at ECS Fall Meeting, Cancun, Mexico, 2006.
- (30) Antolini, E.; Salgado, J. R. C.; Gonzalez, E. R. *J. Power Sources* **2006**, *160*, 957–968.
- (31) Shukla, A. K.; Raman, R. K.; Choudhury, N. A.; Priolkar, K. R.; Sarode, P. R.; Emura, S.; Kumashiro, R. *J. Electroanal. Chem.* **2004**, *563*, 181–190.
- (32) Thompson, D. In *Handbook of Fuel Cells - Fundamentals, Technology and Applications*; Vielstich, W.; Lamm, A.; Gasteiger, H. A., Eds.; Wiley: New York, 2003; Vol. 3, Chapter 37, p 467.
- (33) Watanabe, M.; Tsurumi, K.; Mizukami, T.; Nakamura, T.; Stonehart, P. *J. Electrochem. Soc.* **1994**, *141*, 2659–2668.
- (34) Paulus, U. A.; Wokaun, A.; Scherer, G. G.; Schmidt, T. J.; Stamenkovic, V.; Markovic, N. M.; Ross, P. N. *Electrochim. Acta* **2002**, *47*, 3787–3798.
- (35) Paulus, U. A.; Wokaun, A.; Scherer, G. G.; Schmidt, T. J.; Stamenkovic, V.; Radmilovic, V.; Markovic, N. M.; Ross, P. N. *J. Phys. Chem. B* **2002**, *106*, 4181–4191.
- (36) Teliska, M.; Murthi, V. S.; Mukerjee, S.; Ramaker, D. E. *J. Electrochem. Soc.* **2005**, *152*, A2159–A2169.
- (37) Travitsky, N.; Rippenbein, T.; Golodnitsky, D.; Rosenberg, Y.; Burshtein, L.; Peled, E. *J. Power Sources* **2006**, *161*, 728–789.
- (38) Xiong, L.; Manthiram, A. *J. Mater. Chem.* **2004**, *14*, 1454–1460.
- (39) Salgado, J. R. C.; Antolini, E.; Gonzalez, E. R. *Appl. Catal., B* **2005**, *57*, 283–290.
- (40) Salgado, J. R. C.; Antolini, E.; Gonzalez, E. R. *J. Phys. Chem. B* **2004**, *108*, 17767–17774.
- (41) Antolini, E.; Salgado, J. R. C.; Giz, M. J.; Gonzalez, E. R. *Int. J. Hydrogen Energy* **2005**, *30*, 1213–1220.
- (42) Lima, F. H. B.; Lizcano-Valbuena, W. H.; Teixeira-Neto, E.; Nart, F. C.; Gonzalez, E. R.; Ticianelli, E. A. *Electrochim. Acta* **2006**, *52*, 385–393.
- (43) Schmidt, T. J.; Gasteiger, H. A.; Staeb, G. D.; Urban, P. M.; Kolb, D. M.; Behm, R. J. *J. Electrochem. Soc.* **1998**, *145*, 2354–2358.
- (44) Merzougui, B.; Swathirajan, S. *J. Electrochem. Soc.* **2006**, *153*, A2220–A2226.
- (45) ICDD: International Center for Diffraction Data - Power Diffraction File (PDF) 2 data CD. <http://www.icdd.com/> (accessed 2002).
- (46) Xiong, L.; Manthiram, A. *J. Electrochem. Soc.* **2005**, *152*, A697–A703.
- (47) Arico, A. S.; Shukla, A. K.; Kim, H.; Park, S.; Min, M.; Antonucci, V. *Appl. Surf. Sci.* **2001**, *172*, 33–40.
- (48) *Electrocatalysis*; Lipkowsky, J.; Ross, P. N., Eds.; Wiley-VCH: New York, 1998.
- (49) Markovic, N. M.; Ross, P. N. *Surf. Sci. Rep.* **2002**, *45*, 117.
- (50) Markovic, N. M.; Schmidt, T. J.; Stamenkovic, V.; Ross, P. N. *Fuel Cells* **2001**, *1*, 105.
- (51) Cullity, B. D.; Stock, S. R. *Elements of X-ray diffraction*; 3rd ed.; Prentice Hall: New York, 2001.
- (52) Warren, B. E. *X-ray Diffraction*; Addison-Wesley: Reading, MA, 1969.
- (53) Markovic, N. M.; Gasteiger, H. A.; Grgur, B. N.; Ross, P. N. *J. Electroanal. Chem.* **1999**, *467*, 157–163.
- (54) Masel, R. I. *Principles of Adsorption and Reaction on Solid Surfaces*; Wiley: New York, 1996.
- (55) Somorjai, G. A. *Introduction to Surface Chemistry and Catalysis*; Wiley: New York, 1994.
- (56) Markovic, N.; Gasteiger, H.; Ross, P. N. *J. Electrochem. Soc.* **1997**, *144*, 1591.
- (57) Uribe, F. A.; Springer, T. E.; Gottesfeld, S. *J. Electrochem. Soc.* **1992**, *139*, 765.
- (58) Schmidt, T. J.; Gasteiger, H. A.; Stab, G. D.; Urban, P. M.; Kolb, D. M.; Behm, R. J. *J. Electrochem. Soc.* **1998**, *145*, 2354–2358.
- (59) Sonderberg, J. N.; Sirk, A. H.; Campell, S. A.; Birss, V. I. *J. Electrochem. Soc.* **2005**, *152*, A2017–A2022.
- (60) Stamenkovic, V.; Schmidt, T. J.; Ross, P. N.; Markovic, N. M. *J. Phys. Chem. B* **2002**, *106*, 11970–11979.
- (61) Ralph, T. R.; Hogarth, M. P. *Platinum Met. Rev.* **2002**, *46*, 3.
- (62) Yu, P.; Pemberton, M.; Plasse, P. *J. Power Sources* **2005**, *144*, 11.
- (63) Bonakdarpour, A.; Wenzel, J.; Stevens, D. A.; Sheng, S.; Monchesky, T. I.; Lobel, R.; Atanasoski, R. T.; Schmoegel, A. K.; Vernstrom, G. D.; Debe, M. K.; Dahn, J. R. *J. Electrochem. Soc.* **2005**, *152*, A61.
- (64) Protsailo, L.; Haug, A. *Electrochemical Society Meeting Abstracts*; 208th ECS Meeting Los Angeles, CA, 2005; The Electrochemical Society: Los Angeles, CA, 2005; Vol. abstract 1023.
- (65) Yang, H.; Vogel, W.; Lamy, C.; Vante, N. A. *J. Phys. Chem. B* **2004**, *108*, 11024.
- (66) Xie, J.; Wood, D. L.; Wayne, D. M.; Zawodzinski, T. A.; Atanasov, P.; Borup, R. L. *J. Electrochem. Soc.* **2005**, *152*, A104.
- (67) Li, W.; Zhou, W.; Li, H.; Zhou, Z.; Zhou, B.; Sun, G.; Xin, Q. *Electrochim. Acta* **2004**, *49*, 1045.
- (68) Shukla, A. K.; Neergat, M.; Bera, P.; Jayaram, V.; Hegde, M. S. *J. Electroanal. Chem.* **2001**, *504*, 111–199.
- (69) Shukla, A. K.; Raman, R. K.; Choudhary, N. A.; Priolkar, K. R.; Sarode, P. R.; Emura, S.; Kumashiro, R. *J. Electroanal. Chem.* **2004**, *563*, 181–190.
- (70) Shukla, A. K.; Raman, R. K.; Choudhury, N. A.; Priolkar, K. R.; Sarode, P. R.; Emura, S.; Kumashiro, R. *J. Electroanal. Chem.* **2004**, *563*, 181–190.
- (71) Markovic, N. M.; Grgur, B. N.; Lucas, C. A.; Ross, P. N. *J. Phys. Chem. B* **1999**, *103*, 487.